Self-assembly synthesis of boron-doped graphitic carbon nitride hollow tubes for enhanced photocatalytic NOx removal under visible light

Zhenyu Wang[a,b], Meijuan Chen[a], Yu Huang[b,c,*], Xianjin Shi[b,c], Yufei Zhang[b,c], Tingting Huang[b,c], Junji Cao[a,b,c,*], Wingkei Ho[d], Shun Cheng Lee[e]

[a] School of Human Settlements and Civil Engineering, Xi'an Jiaotong University, Xi'an, 710049, China
[b] Key Lab of Aerosol Chemistry & Physics, Institute of Earth Environment, Chinese Academy of Sciences, Xi'an, 710061, China
[c] State Key Labof Loess and Quaternary Geology (SKLLQG), Institute of Earth Environment, Chinese Academy of Sciences, Xi'an, 710061, China
[d] Department of Science and Environmental Studies, The Hong Kong Institute of Education, Hong Kong, China
[e] Department of Civil and Environmental Engineering, The Hong Kong Polytechnic University, Hung Hom, Hong Kong, China

ABSTRACT

Oriented transfer of electron-hole charge carriers is important during photocatalytic processes. In this study, one-dimensional (1D) tubular B-doped graphitic carbon nitride (g-C_3N_4) with an effective charge transfer and separation was designed. The doping sites, energy level structure, and photo-generated electron-hole pair separation were predicted using systematical density functional theory (DFT) simulations. The supramolecular precursor for tubular g-C_3N_4 synthesis, namely melamine·cyanuric acid (M·CA), was controllably synthesized from a single melamine source. Intermolecular hydrogen bonding led to the arrangement of supramolecular aggregate structures into a prismatic crystal architecture during the hydrothermal treatment. The morphology modulation of g-C_3N_4 from bulk to 1D tubular architecture was realized by calcining the prism-like precursor. B-doped tubular g-C_3N_4 exhibited a narrower band-gap, multiple reflections of incident light, and oriented transfer of electron-hole charge carriers, which led to a widened light-harvesting range and improved photo-induced electron-hole pair separation and transfer ability. These factors contributed to the photocatalytic activity enhancement towards gaseous NO_x degradation under visible light. In this work, a valuable design-fabrication pattern for g-C_3N_4 modification and engineering via DFT simulations was designed. Moreover, a strategy was developed for the simultaneous foreign atom doping and architecture control of g-C_3N_4 via the self-assembly of supramolecular precursors.

1. Introduction

The NO_x pollutants continue to accumulate in the atmosphere, causing the frequent occurrence of heavy haze events [1]. However, selective catalytic reduction, three way catalysis et al. are effective abatement approaches for NO_x removal from emission source (ppm), but not suitable for NO_x removal at ambient concentration levels (ppb) [2]. Photocatalysis is a green and simple alternative for NO_x degradation at even ppb levels, due to the advantages of using abundant solar energy and ambient working conditions [3–7]. The metal-free semiconductor photocatalyst graphitic carbon nitride (g-C_3N_4) has attracted a great deal of attention for the removal of haze precursors, especially NO_x, due to its fascinating conjugated structure, visible-light response, and earth-abundant nature [8–10]. However, because of its limited visible-light harvesting ability and poor separation and transfer abilities

of the photo-excited electron-hole pairs, pristine g-C_3N_4 cannot achieve sufficiently efficient NO_x removal unless modified by morphology engineering, element doping, or heterostructure construction [10].

Recently, 1D tubular structures with well-defined interior voids and functional shells have attracted increasing attention because they exhibit improved light-harvesting capacity via multiple reflection of incident light within the interior voids and the advantage of oriented electron transfer compared to that of the bulk structure [11–14]. For example, Li et al. synthesized a hollow TiO_2 architecture exhibiting greatly enhanced photocatalytic degradation activity compared to that of the nonporous one, owing to the enhanced absorption efficiency caused by multiple reflections present inside the pores [15]. Furthermore, Mor et al. found that TiO_2 tubes act as electron highways and thereby exhibit superior electron transport capability due to the 1D tubular architecture [16]. Therefore, considering the limited light-

---

harvesting and photo-excited electron-hole pairs transfer abilities of the bulk g-C$_3$N$_4$, morphology engineering of bulk to 1D tubular structure should be an effective approach to satisfy the improvement of light-harvesting and photo-excited charge carrier transfer simultaneously. Current approaches to the preparation of g-C$_3$N$_4$ tubular structures usually involve soft or hard templating. These approaches lead to texture modifications and specific surface area enlargements but involve tedious steps, harsh conditions, introduction of impurities, and sometimes extremely hazardous, toxic, and environmentally harmful fluoride-containing template etchants [10,17,18]. Recently, the formation of a supramolecular preassembly of an melamine·cyanuric acid (M·CA) complex precursor has become an interesting self-templating method to alter the optical and textural features of g-C$_3$N$_4$ [19,20]. The intermolecular hydrogen bonding can play the role of an extra template to produce ordered molecular building blocks by arranging the supramolecular aggregate structures. Thus, the self-assemble strategy is regarded as a simple and reliable method to engineer the morphology and structure of materials. One of the pioneer studies in the subject reported that the melamine complex and its ramification could form a prismatic crystal architecture after a hydrothermal treatment [21]. Therefore, it is feasible to obtain a 1D g-C$_3$N$_4$ tubular structure by calcining the prismatic supramolecular precursor. Currently, there are several reports on the fabrication of tubular g-C$_3$N$_4$ through supramolecular pre-organization and linking M with the CA. For example, Guo et al. reported the formation of g-C$_3$N$_4$ tubes with a layered micro-nanostructure using a rod-like M·CA precursor [22]. These tubes showed a more superior hydrogen evolution performance than that shown by pristine g-C$_3$N$_4$. Later, Tong et al. synthesized a tubular g-C$_3$N$_4$ isotype heterojunction by calcining the hydrothermally treated M·CA precursor [23]. It was also found that the photo-production electrons are transferred along the longitudinal dimension due to the tubular structure, while the recombination rate is still high. It is a well-known fact that melamine could be transformed into cyanuric acid spontaneously under suitable conditions. However, few researchers have taken advantage of this peculiarity of melamine and synthesized in situ an M·CA supramolecular precursor.

Because of its widened light-harvesting range and effective photo-induced charge carrier separation, element doping has proven to be an indispensable strategy for band-gap narrowing and electronic structure realignment. Incorporating suitable foreign atoms into a crystal frame can effectively modulate the band-gap of semiconductors through an atomic orbital hybridization. Asahi and his co-workers were the first to introduce a nitrogen element into TiO$_2$. The obtained TiO$_{2-x}$N$_x$ compound exhibits an improved light harvesting under visible light compared to that obtained with TiO$_2$. This is because the N p states contribute to the band-gap narrowing by mixing with the O 2p states [24]. In addition, incorporating foreign elements into the g-C$_3$N$_4$ frame is a feasible strategy to reduce the recombination rate due to the electronic polarization effects [25–34]. Recently, Huang et al. successfully fabricated g-C$_3$N$_4$ using an O-substitutional doping and found that the separation of the electron-hole pairs is improved by charge redistribution around the dopant [35]. Therefore, element doping seems to be a good method to simultaneously achieve band-gap engineering and effective photo-induced charge carrier separation. Among the various dopants, boron (B) has a similar size and chemical properties to the carbon atom. B-C containing functional groups could act as Lewis acid sites. Therefore, the boron atom from the B-doped g-C$_3$N$_4$, prepared via an atom replacement, can function as an exciton dissociation trap or an adsorption site in a photocatalytic process [29]. The Wang group reported a B-modified g-C$_3$N$_4$ exhibiting a narrow band-gap (2.88–2.83 eV), but did not provide an in-depth analysis [29]. Hitherto, many studies on the B-doped g-C$_3$N$_4$ have been extensively reported [29,36]. However, these lack morphology design and engineering, and often employ organic boron sources such as sodium tetraphenyl boron (Ph$_4$BNa), which may introduce extra impurities like C and Na. Therefore, preparing g-C$_3$N$_4$ simultaneously with a 1D tubular architecture and B element

doping is highly desirable and could enhance the simultaneous light-harvesting ability, photo-excited electron-hole pair separation, and transfer abilities of pristine bulk g-C$_3$N$_4$. However, in order for this goal to be achieved, many challenges need to be overcome.

In this study, we systematically applied DFT simulations as ideal guides to the design and, eventually, the controlled synthesis of hollow B-doped g-C$_3$N$_4$ tubes. The synthesis was obtained by calcining self-assembly supramolecular precursors, obtained by the self-conversion of a single melamine source with the help of boric acid. Unlike the usual role of DFT simulations to only serve as assistant tools to prove experimental results, in this study we adequately utilized the predictability of DFT simulations to controllably design materials instead of using the trial-and-error method. The prepared B-doped hollow tubular g-C$_3$N$_4$ exhibited an obviously improved photocatalytic activity for NO degradation under visible-light irradiation compared to the bulk g-C$_3$N$_4$ and pure hollow tubular g-C$_3$N$_4$. This effect was caused by the superior light-harvesting, photo-generated electron-hole pair separation, and charge-carrier transfer abilities. Furthermore, we looked into the mechanisms of supramolecular precursor formation and tubular structural evolution of B-doped g-C$_3$N$_4$. Additionally, mechanisms of photocatalytic NO-removal and activity enhancement over the tubular B-doped g-C$_3$N$_4$ were proposed.

2. Experimental Section

2.1. Computational mode

First, g-C$_3$N$_4$ was modeled using a $(1 \times 1 \times 1)$ unit cell for predicting the most possible B doping form (substitutional or interstitial doping) and doping sites (Fig. S1, Supporting information). Subsequently, a $(3 \times 2 \times 1)$ supercell (including 168 atoms) before and after one B atom doping at the C1 site was built according to the results of the XPS on the further total density of state (TDOS), partial density of state (PDOS) and electron density difference (EDD) calculations (Fig. S2, Supporting information).

All calculations were performed in the DFT framework using the Cambridge Sequential Total Energy Package (CASTEP) in Material Studio 8.0. [37]. The generalized gradient approximation (GGA) with revised Perdew-Burke-Ernzerhof (PBE) was adopted for the exchange-correlation function [38,39]. In this framework, a large convergence of the plane-wave expansion was obtained with an energy cut-off of 380 eV. In order to optimize the geometry of the $(1 \times 1 \times 1)$ unit cell, the Brillouin zone was sampled in a $(2 \times 2 \times 2)$ Monkhorst-Pack k point grid [40]. For geometry optimization, DOS, and EDD of the $(3 \times 2 \times 1)$ unit cell, a $(1 \times 2 \times 3)$ Monkhorst-Pack k point was used. The geometries were not optimized until the energy, force and maximum displacement converged to 5.0×10^{-6} eV/atom, 1×10^{-2} eV/Å, and 5×10^{-4} Å, respectively. The spin polarization was considered throughout all calculations. In addition, the aim of the EDD calculation was to clarify the charge transfer based on the Mulliken population [41].

To compare the relative stability of different doping forms and sites in g-C$_3$N$_4$, the formation energy E_f of the substitutional doped systems was estimated according to Eq. (A1):

$$E_f = E_{dope} + \mu_X - E_{pure} - \mu_B \tag{A1}$$

The formation energy E_f of the interstitially doped systems was estimated according to Eq. (A2):

$$E_f = E_{dope} - E_{pure} - \mu_B \tag{A2}$$

where E_{dope} is the total energy of g-C$_3$N$_4$ containing the impurity, E_{pure} is the total energy of the pure g-C$_3$N$_4$ system, μ_X is the chemical potential of the C or N atom obtained from the C bulk model and N$_2$ molecule, respectively, and μ_B is the chemical potential of the B atom calculated from the bulk model. Here, the more negative the defect

formation energy was, the more facile the doping was.

2.2. Synthesis of B-doped tubular g-C$_3$N$_4$ samples

All chemicals were used without further purification. In a typical process, 1 g melamine was completely dissolved in 70 mL deionized water at 60 °C under vigorous stirring for 1 h. Then, 1, 2, 3 mmol H$_3$BO$_3$ was added to the resulting solution, respectively. After stirring rigorously for 30 min, the mixture was transferred into a 100 mL Teflon-lined autoclave and heated at 180 °C for 8 h. After cooling down to room temperature naturally, the products were filtrated, washed thoroughly three times with deionized water and absolute ethanol, and subsequently dried at 60 °C for 12 h. Finally, the products were heated to 500 °C for 3 h under a flow of nitrogen with a heating rate of 2.5 °C/min. The resulting materials were designated as BCNT-1, BCNT, BCNT-3, respectively. For comparison, g-C$_3$N$_4$ was synthesized in the same way without H$_3$BO$_3$ and denoted as CNT. Bulk g-C$_3$N$_4$ directly represented melamine, which underwent no hydrothermal process and was denoted as CN. The BCNT was chosen as the representative of B-doped tubular g-C$_3$N$_4$ because of the optimal NO removal efficiency (Fig. S3a, Supporting information) and the inhibition of NO$_2$ production (Fig. S3b, c, Supporting information).

2.3. Characterization methods

The crystal phase was analyzed via X-ray diffraction (XRD) with Cu Kα radiation at a scan rate of 0.05° 2θ/s (λ = 1.5406 Å, 40 kV, 40 mA, PANalytical X'Pert PRO X-ray diffractometer). Samples were embedded in KBr pellets and then subjected to Fourier-transform infrared spectroscopy (FT-IR) on an FT-IR absorption spectrometer (Magna-IR 750, Nicolet, USA). X-ray photoelectron spectroscopy (XPS) was conducted using an X-ray photoelectron spectrometer (Thermo ESCALAB 250, USA). All binding energies were calibrated to the C 1s peak of the surface adventitious carbon at 284.8 eV. Scanning electron microscopy (SEM, JEOL JSM-6490, Japan) was used to characterize the morphology and elemental distribution maps of the obtained products. Transmission electron microscopy (TEM) was performed using a JEOL JEM-2100HR CM-120 (Japan) transmission electron microscope. Moreover, a nitrogen adsorption apparatus (ASAP 2020, USA) was used to obtain the BET of the samples that were degassed at 250 °C prior to analysis. A Varian Cary 100 Scan UV–vis system equipped with a Labsphere diffuse reflectance accessory was used to obtain the reflectance spectra of the catalysts over a range of 200–800 nm. Labsphere USRS-99-010 was employed as a reflectance standard. Photoluminescence and time-resolved fluorescence emission spectra (PL, FLS980, Edinburgh, England) were obtained to investigate the lifetime of the photo-induced charges, and the optical properties of the resulting samples. The intermediate and final products, nitrate and nitrite ions, were extracted by immersing the powders (about 0.05 g) into 6 mL deionized water and measured by using a Dionex-600 Ion Chromatograph (IC, Dionex Inc., Sunny-vale, CA, USA) after the photocatalytic activity test equipped with an IonPac AS14 A column. Samples for the electron spin-resonance spectroscopy (ESR, ER200-SRC, Bruker, Germany) were prepared by mixing 0.05 g of the as-prepared photocatalyst in a 25 mM 5,5′-dimethyl-1-pyrroline-*N*-oxide (DMPO) solution. Measurements were prepared with a 50 mL aqueous dispersion for DMPO-•OH and a 50 mL alcohol dispersion for DMPO-·O$_2^-$ under irradiation with 420 nm visible-light.

2.4. Photoelectrochemical measurements

The photoelectrochemical properties of the as-prepared samples were evaluated using a Parstat 4000 electrochemical workstation (USA) in a conventional three-electrode cell, with a platinum plate and an Ag/AgCl electrode as the counter and reference electrodes, respectively. The photocurrent-time curves were measured at 0.2 V vs. Ag/AgCl in

0.5 mol/L Na$_2$SO$_3$ at ambient temperature under a 300 W Xe lamp (MicroSolar 300, Perfectlight, China) with a UV cutoff filter (420 nm). Electrochemical impedance spectroscopy (EIS) was measured at a frequency range of 0.1 Hz to 100 kHz with a 5 mV voltage amplitude under an open-circuit voltage in a 1 mmol/L K$_3$Fe(CN)$_6$ and K$_4$Fe(CN)$_6$ solution. For the Mott-Schottky (M–S) measurements, the working electrode was immersed in a 0.1 M Na$_2$SO$_4$ aqueous solution (pH 12), and subjected to 5 mV perturbation bias at fixed frequency of 1 kHz from -0.6 to 0.8 V vs. Ag/AgCl.

2.5. Photocatalytic activity test

The photocatalytic activity of the as-prepared samples was investigated in terms of NO removal at ppb levels in a continuous flow reactor system at ambient temperature. The rectangular reactor, which was fabricated from stainless steel and covered with quartz glass, possessed a volume capacity of 4.5 L (30 cm × 15 cm × 10 cm). A 300 W commercial Xe arc lamp (MicroSolar 300, Perfectlight, China) was vertically placed outside the reactor. UV light in the light beam was removed by adopting a UV cutoff filter (420 nm). The photocatalyst (0.1 g) was coated onto a dish (10.0 cm in diameter), which was subsequently heated at 60 °C to remove any water in the suspension. NO gas was supplied by a compressed gas cylinder at a concentration of 48 ppm (N$_2$ balance) in accordance with the standard of the National Institute of Standards and Technology. The initial NO concentration was diluted to 400 ppb by an air stream supplied by a zero-air generator (Model 1001, Sabio Instruments LLC, Georgetown, TX, USA), and the flow rate was maintained at 3 L/min. The lamp was turned on when the adsorption-desorption equilibrium was achieved and the optical power density reaching the sample surface was calibrated to be 25.46 mW/cm^2 using an optical power meter (Thorlabs PM100D Optical Power Meter). The concentration of NO was continuously measured using a chemiluminescence NO analyzer (Model 42c, Thermo Environmental Instruments Inc., Franklin, MA, USA). This apparatus monitored the concentrations of NO and NO$_2$ at a sampling rate of 0.6 L/min. The removal ratio (η) of NO was calculated as η (%) = (1 − C/C$_0$) × 100, where C and C$_0$ were the concentrations of NO in the outlet and feeding streams, respectively.

3. Results and discussion

3.1. B-doping site prediction, phase structure, and chemical composition of BCNT

First, DFT theoretical calculations were performed on the g-C$_3$N$_4$ primitive cell establishment and the structure was optimized using CASTEP (Fig. S1a, Supporting information). Then, different sites were explored for the boron atom substitution doping: three inequivalent nitrogen sites (N1, N2, and N3, Fig. S1b, Supporting information), and two inequivalent carbon sites (C1 and C2, Fig. S1b, Supporting information). Additionally, interstitial doping at pore or interlamination was attempted (Fig. S1c, Supporting information). These structures were built by introducing one boron atom to each doping site and subsequently preforming a geometry optimization. The pristine C–N (Fig. 1a) bonds were slightly stretched after the B substitution on the N or C site, forming B–N (Fig. 1b) and B–C (Fig. 1c) bonds. A different degree of deformation occurred after the B-doping at pore and interlayer (Fig. 1d) due to the re-arrangement of the electronic structure. In order to evaluate the most probable doping mode, the formation energies of all modes were calculated. As shown in Table S1 (Supporting information), the substitutions at the C sites were much more favorable than the N-site substitutions and interstitial doping. From these results, the C1 site substitutional doping with the lowest formation energy (-7.56 eV) was recognized as the optimal boron doping site.

In order to verify the accuracy of the DFT predictions, the phase structures and chemical compositions of pristine g-C$_3$N$_4$ (CN), tubular
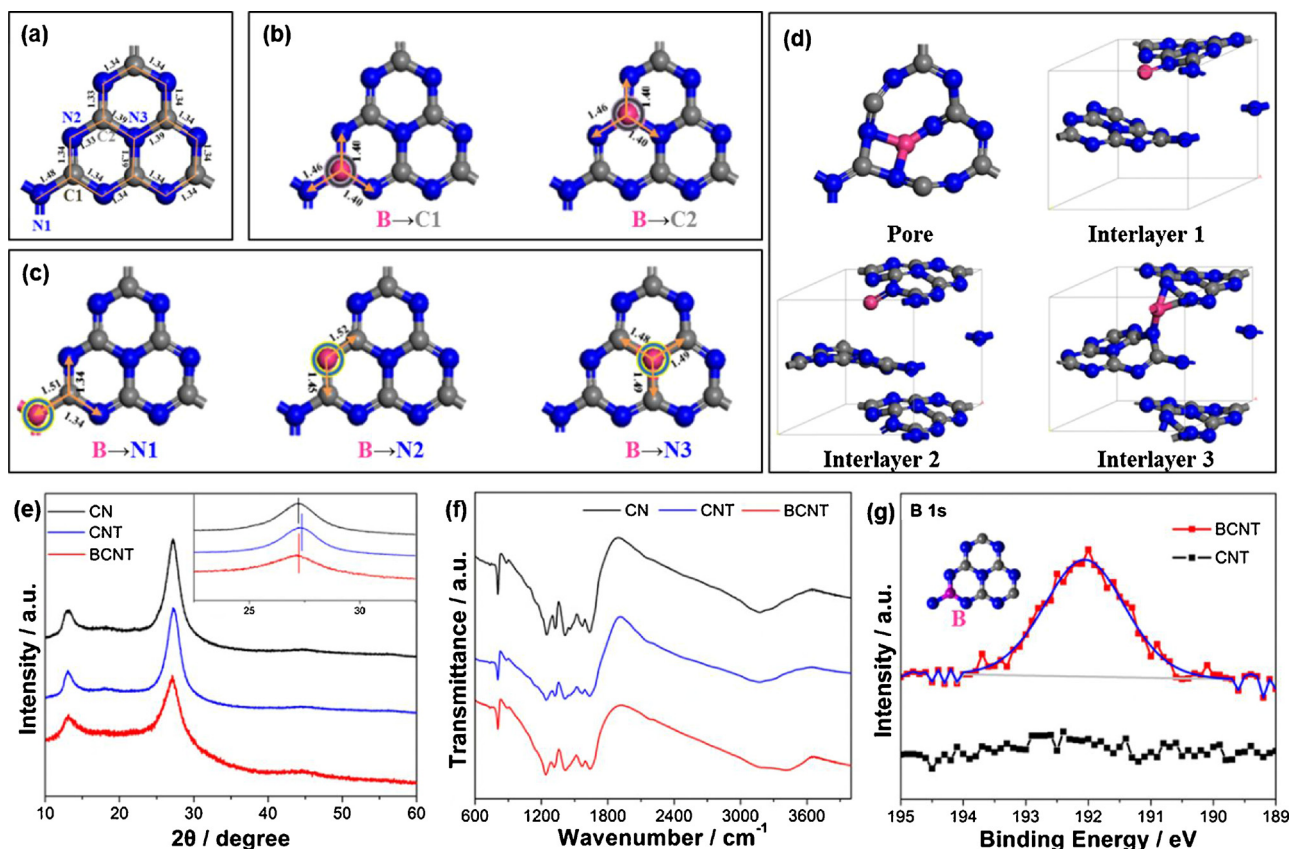
Fig. 1. (a) Pristine g-C$_3$N$_4$ mode. Boron atom substitution doping at (b) two inequivalent carbon sites or (c) three inequivalent nitrogen sites. (d) Interstitial doping at pore or interlayers. All samples underwent a subsequent geometry optimization. (e) XRD patterns (The small inset represents the (002) peaks of all samples after enlargement) and (f) FT-IR spectra of CN, CNT, and BCNT. (g) XPS high-resolution spectra of B 1 s for BCNT and CNT.

g-C$_3$N$_4$ (CNT), and B-doped tubular g-C$_3$N$_4$ (BCNT) were investigated. Fig. 1e shows an X-ray diffraction pattern of the obtained CN, CNT, and BCNT samples. The two typical diffraction peaks centered at around 13.0° and 27.6° were attributed to the intralayer long-range order tri-s-triazine units and interlayer stacking of the aromatic units of CNT, respectively [8]. When the B atoms were introduced, the (002) peaks slightly shifted from 27.3° of CNT to 27.1° of BCNT (inset of Fig. 1e), indicating that the distance of the interlayer stacking of the aromatic units increased slightly because of the B dopant disturbance. The FT-IR spectra of all samples showed similar characteristic bands of g-C$_3$N$_4$. More specifically, the band at 810 cm^{-1} belonged to the breathing mode of the heptazine ring system, the bands at 1200-1600 cm^{-1} were from the stretching vibration of the aromatic CN heterocycles, and the band at 3000-3600 cm^{-1} were because of the primary and secondary amines (Fig. 1b). [9] However, the vibration of B−N typically appearing at 1370 cm^{-1} was not distinguished, due to an overlap with the C−N stretching band.

The surface compositions and electronic structures of the B, C, and N atoms in CNT and BCNT were verified using X-ray photoelectron spectroscopy (XPS). In the B 1 s spectra, there was a binding energy peak centered at 192.0 eV for BCNT, which was not detected for CNT (Fig. 1g). This peak was assigned to a typical N-B−N coordination, which is higher than that of h-BN (190.0 eV) and lower than that of Kawaguchi's boron carbon nitride BCN(H) (192.1 eV, in which boron is surrounded by three nitrogen atoms) [42]. This suggests that the boron atoms were introduced into the CN matrix by substituting the carbons at the C1 sites in accordance with the predictions from the DFT calculations. The concentration of the B atom in BCNT was 0.6 At%. For the C 1 s spectrum in Fig. S4a (Supporting information), the binding energy peaks located at 288.4, 286.2, and 284.8 eV were assigned to C-N -C (A1), (C)$_3$-N (A2) for BCNT and CNT, and adventitious C-C,

respectively [43]. With the introduction of B into the molecule, the peak-area ratio of A1/A2 decreased from 5.91 (CNT) to 4.78 (BCNT) due to the fact that part of the C-N -C structure on the surface was replaced by a C-N -B structure. The main signals in the N 1 s spectrum in Fig. S4b (Supporting information) occurred around 401.2, 399.9, and 398.5 eV for both BCNT and CNT. These peaks were assigned to the N−H groups, tertiary nitrogen N-(C)$_3$ groups, and C–N-C groups, respectively [43]. No obvious N−B group (399.2 eV) signal was detected for BCNT due to its small content and the fact that its binding energy could overlap with that of other N-containing groups. Meanwhile, the positions of both C 1 s and N 1 s for BCNT were slightly shifted compared to these of CNT, which suggests that the electron structure of BCNT changed because of the B doping. According to results presented above, it can be concluded that the position of the dopant atoms can be accurately foreseen by the DFT theoretical calculations, providing a reliable guide for the designations of element doping forms and sites.

3.2. Morphological structure, texture property, and morphology evolution

SEM images of the supramolecular BCNT precursor showed that it exhibits a hexagonal prism-like rod structure with a length up to dozens of microns and a diagonal of 2 μm (Fig. 2a). Normally, melamine needs cyanuric acid to form a supramolecular structure. However, we found that supramolecular aggregates (JCPDS: 05-0127) [19] were formed by single melamine sources (JCPDS: 24-1923) [44] and the addition of H$_3$BO$_3$ after the opportune hydrothermal treatment did not have any effect on the formation (Fig. S5a, Supporting information). In particular, M partially transformed into CA, while the remaining one combined with the in-situ-generated CA to form an M·CA supramolecular structure. This hypothesis was further confirmed by FT-IR spectroscopy (Fig. S5b, Supporting information). The spectrum of commercial
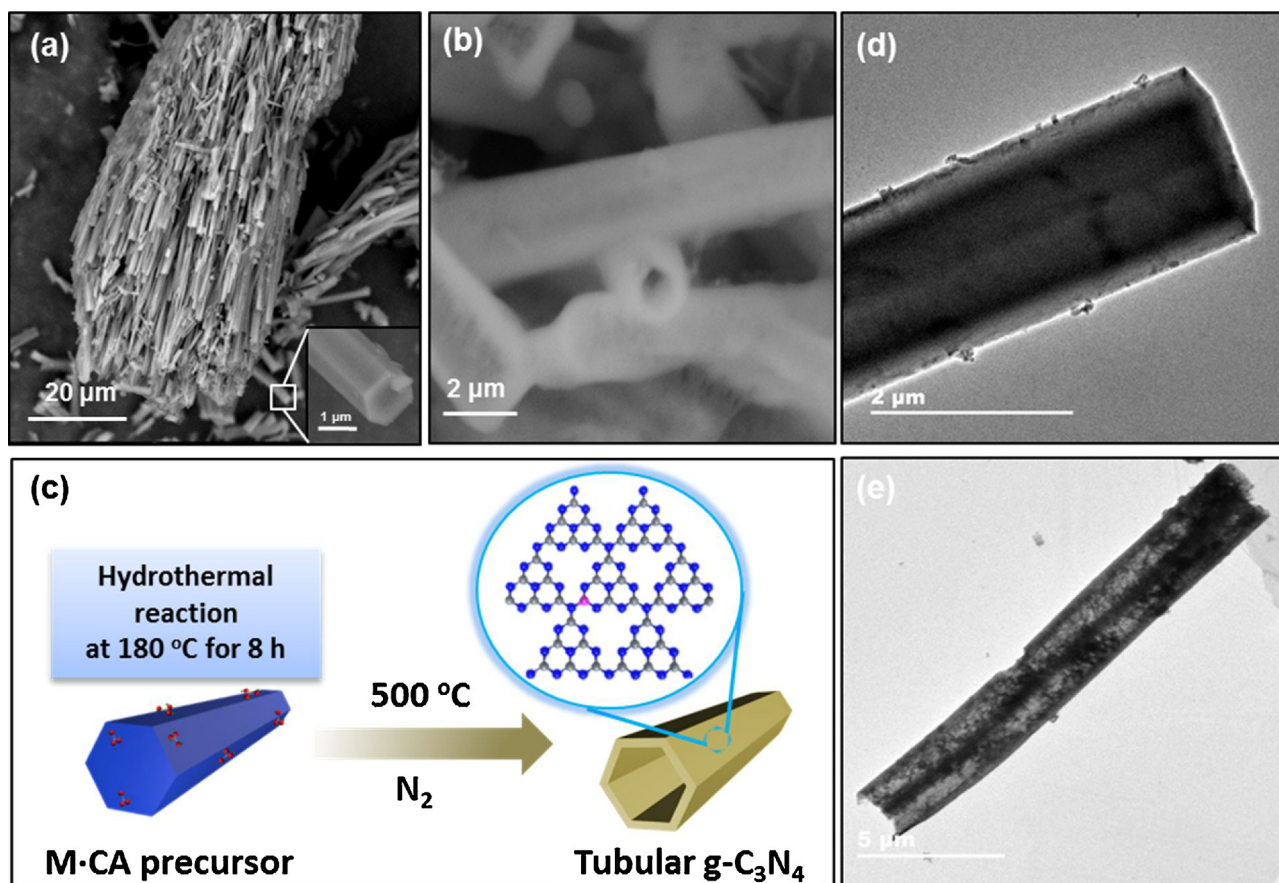
Fig. 2. SEM images of (a) the BCNT precursor, and (b) BCNT. (c) Schematic diagram of the process of tubular BCNT formation. TEM images of (d) the BCNT precursor, and (e) BCNT.

melamine showed peaks at 3469 and 3419 cm^{-1}, which were attributed to the NH$_2$ stretching vibration, and peaks at 3331 and 3128 cm^{-1}, which were ascribed to the asymmetric and symmetric stretching vibrations of N−H respectively [19]. In contrast, the cyanuric acid spectrum showed a peak at 1720 cm^{-1} that belonged to the C═O stretching vibration [45]. Concerning the CNT and BCNT precursors, the N−H deformation vibrations and C–N stretching vibrations were located at 1655 and 1028 cm^{-1}, respectively. However, these were weakened compared to the ones in melamine, which indicated the rearrangement of the molecular structure [35]. The shift of the C═O stretching vibration from 1720 to 1730 cm^{-1} suggests that part of the melamine converted to cyanuric acid and a hydrogen bond (N–H…O) was formed between the remaining melamine and the in-situ-transformed cyanuric acid. In contrast, the triazine ring vibration intensity reduced from 813 to 783 cm^{-1} because of a hydrogen bonding of N–H…N [19]. The aforementioned XRD and FT-IR results indicated that cyanuric acid can be formed in-situ through a single melamine source, and the supramolecular precursor of g-C$_3$N$_4$ can be synthesized simultaneously during the hydrothermal process.

After calcination at 500 °C under N$_2$ atmosphere, the prism-like rods of BCNT precursor transformed into hollow tube structures of BCNT (Fig. 2b). The elemental mapping images of BCNT sample (Fig. S6a–d) indicated that the B, C and N elements were uniformly distributed all over the B-doped g-C$_3$N$_4$ hollow tube. In contrast, the similar tubular morphologies of CNT and the irregular bulk CN are observed in Fig. S7 (Supporting information). According to results of the study, boron acid molecules were adsorbed on the precursor surface during the hydrothermal process. Subsequently, the B atoms were squeezed into the g-C$_3$N$_4$ frame during the thermal polymerization process (Fig. 2c). According to the corresponding TEM images, the BCNT precursor

exhibited a solid rod architecture (Fig. 2d) and BCNT showed a hollow tubular structure with a 0.3 μm average thickness of the tube wall (Fig. 2e). The nitrogen adsorption-desorption isotherms of CN, CNT, and BCNT were investigated and shown in Figure S8. The results show all samples are of type IV (BDDT classification), suggesting all samples are belong to mesoporous materials [46]. Additionally, the BET specific surface areas of CN, CNT, and BCNT were 17.8, 25.5, and 27.9 m^2/g, respectively. This indicated that the reason for the improved specific surface area was the morphology engineering from bulk to hollow tubular structure, rather than the B doping. The higher specific surface area could provide more active sites for adsorption and surface reaction, which is conducive to the photocatalytic NO$_x$ degradation.

The hydrothermal reaction at 180 °C was monitored over time by detecting the SEM images and XRD patterns of the BCNT supramolecular precursors (Fig. S9, Supporting information). The results displayed the gradual process of the morphology evolution from bulk melamine crystal (0 h, Fig. S9a, Supporting information) to a prism-like supramolecular precursor (8 h, Fig. S9f, Supporting information). It was detected that M maintained its original crystal structure when boron acid molecules were adsorbed on its surface in the beginning of the hydrothermal process (Fig. S9a, Supporting information). With the hydrothermal reaction time prolonged to 2 and 4 h, the M was partially converted in situ to CA, gradually making the surface of the particles rough (Fig. S9b, c, Supporting information). When the reaction was left for 6 h, hexagonal prism-like rods appeared on the surface of the particles (Fig. S9d, Supporting information), which were formed from the molecular self-assembly of M and CA through N–H…O and N–H…N hydrogen bonding. Continuous rod-like structures embedded on the surface of the bulk melamine were observed after the hydrothermal reaction time was prolonged to 7 h (Fig. S9e, Supporting information).
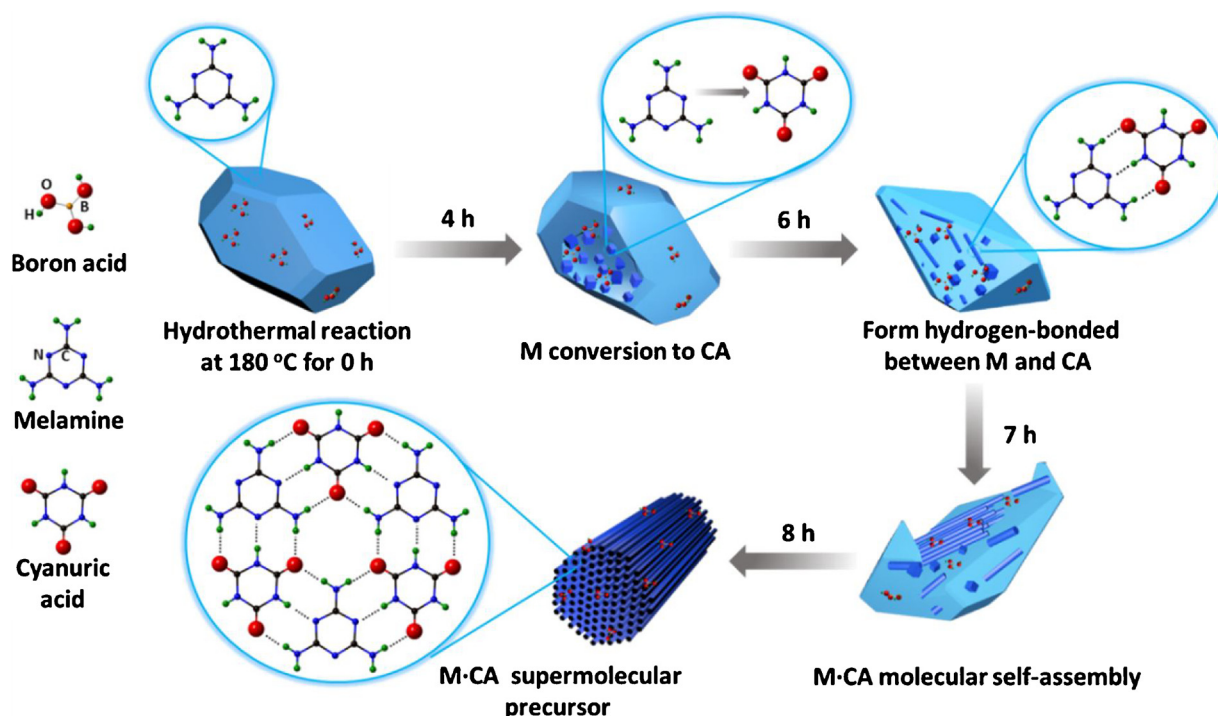
Scheme 1. Schematic diagram of the process of the BCNT precursor morphology evolution during the hydrothermal process with increasing reaction time.

XRD analysis showed that these rod-like structures belonged to the M·CA supramolecular structure. When the reaction time was increased to 8 h, it was found that the hexagonal prism-like rods dominated the structure of the supramolecular precursor, and the boron acid molecules were uniformly distributed on its surface (Fig. S9f, Supporting information). A more vivid time-resolved formation process of the supramolecular precursors is depicted in Scheme 1 .

3.3. Optical properties and band gap structure

DFT calculations were also employed to illustrate the role of B-doping in band gap engineering. The primitive super-cell unit of g-C$_3$N$_4$ and its total density of state (TDOS) and partial density of state (PDOS) are shown in Fig. 3a and b, respectively. The band gap of pristine g-C$_3$N$_4$ was calculated to be 1.16 eV, which was smaller than the experimental value due to the limitations of DFT in underestimating the band gap [35,47]. As shown in Fig. 3b, after B was introduced to the C1 site (B atom doping concentration was approximately 0.6%, Fig. 3a), the band gap narrowed slightly (1.05 eV). Considering the shift down of the conduction band (CB), the absorption band edge appeared red shifted, leading to the enhancement of the visible-light absorption abilitiy. To reveal the contributions of every related orbital to the band, PDOSs were calculated and displayed in Fig. 3b. The valence bands (VBs) of the pristine g-C$_3$N$_4$ and B-doped g-C$_3$N$_4$ were primarily composed of C 2p, N 2 s, and N 2p orbitals. In contrast, the CBs were dominated by C 2p and N 2p orbitals of pristine g-C$_3$N$_4$ and B-doped g-C$_3$N$_4$. After the PDOS enlargement (Fig. 3c), it was observed that the 2p orbital of B hybridized with the C 2p, N 2 s, and N 2p orbitals in the deep energy level of the VB, which had an insignificant effect on the change in the VB top. However, the slight downshift at the bottom of the CB can be attributed to the hybrid of p orbitals formed from the C, N, and B atoms.

Subsequently, the optical absorption ability and band gap of the obtained samples were analyzed by UV–vis diffuse reflectance spectroscopy (Fig. 3d). The absorption edge of CNT was almost the same as the one of CN, while its absorption intensity increased because of the multiple reflections of incident light across the tubular structure. In contrast, BCNT exhibited a small red-shift and increased tail absorption compared to CNT because of the incorporation of B atoms into the g-C$_3$N$_4$ framework and the resulting defect states [29,48]. The band-gaps of the samples were determined through the absorption edge using the Kubelka–Munk method [49] to be 2.70, 2.66, and 2.54 eV for CN, CNT, and BCNT, respectively. Then, the VB edge relative potentials of CN and BCNT were estimated from the XPS valence band spectra. These potentials reflect the energy differences between the Fermi levels and actual VB position [50]. As shown in Fig. S10 (Supporting information), the relative energy levels of the VB of CN and BCNT were uniform, indicating that the B doping had a negligible effect on the change in the energy differences between the Fermi levels and the actual VB position. According to previous reports, g-C$_3$N$_4$ is an n-type semiconductor, which means that the flat band potential lies very close to the bottom of the conduction band [51]. Therefore, Mott-Schottky (M–S) plotting of CN and BCNT was used as a reliable electrochemical method to investigate the position of CB. As can be seen in Fig. 3e, the flat band potentials of CN and BCNT were respectively -1.38 and -1.21 V vs. Ag/AgCl at pH 7 (converted to -1.18 and -1.01 V vs. NHE at pH 7 through the Nernst equation [52]). Combined with the position of CB and the band-gap results, the VB tops of CN and BCNT were calculated to be 1.52 V and 1.53 V, respectively. The changes in the level structure of g-C$_3$N$_4$ after the B doping conform to the DFT predictions. The band structure alignments of CN and BCNT are given in Fig. 3f. The CB of BCNT was lower than that of CN, indicating that more photo-generated charges were formed under the same circumstances, and more ·O$_2^-$ radicals were produced from the O$_2$ trapping process.

Fig. 3(a) Optimized pristine supercell structure (upper structure) and B doped supercell structure with B atom doping concentration of 0.6% at the C1 site (lower structure). (b) Calculated TDOS and PDOS of pristine g-C$_3$N$_4$ and B doped g-C$_3$N$_4$. (c) Enlarged PDOS. (d) UV–vis diffuse reflectance spectra of CN, CNT, and BNCT. (e) Mott-Schottky plots and (f) band structure of CN and BCNT.

3.4. Separation efficiency and transfer ability of electron-hole pairs

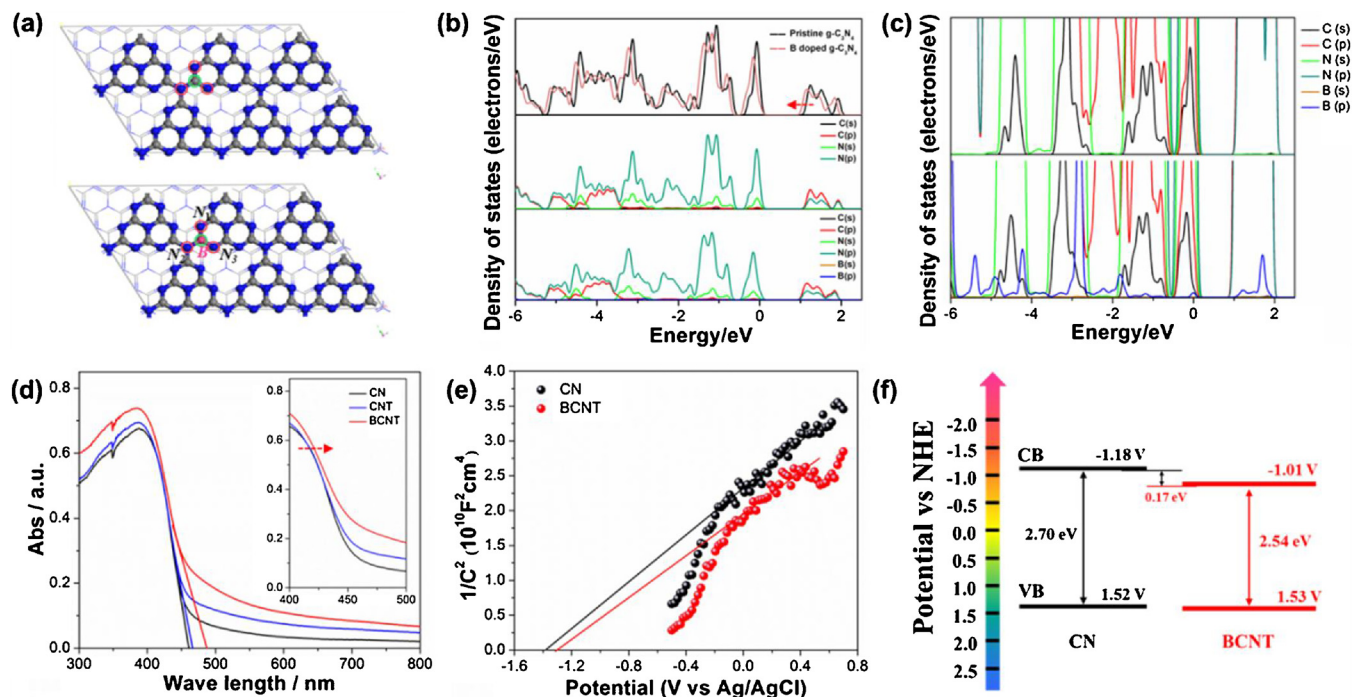To illustrate the change in electron distributions after the B-doping

Fig. 3. (a) Optimized pristine supercell structure (upper structure) and B doped supercell structure with B atom doping concentration of 0.6% at the C1 site (lower structure). (b) Calculated TDOS and PDOS of pristine g-C_3N_4 and B doped g-C_3N_4. (c) Enlarged PDOS. (d) UV–vis diffuse reflectance spectra of CN, CNT, and BNCT. (e) Mott-Schottky plots and band structure of CN and BCNT.
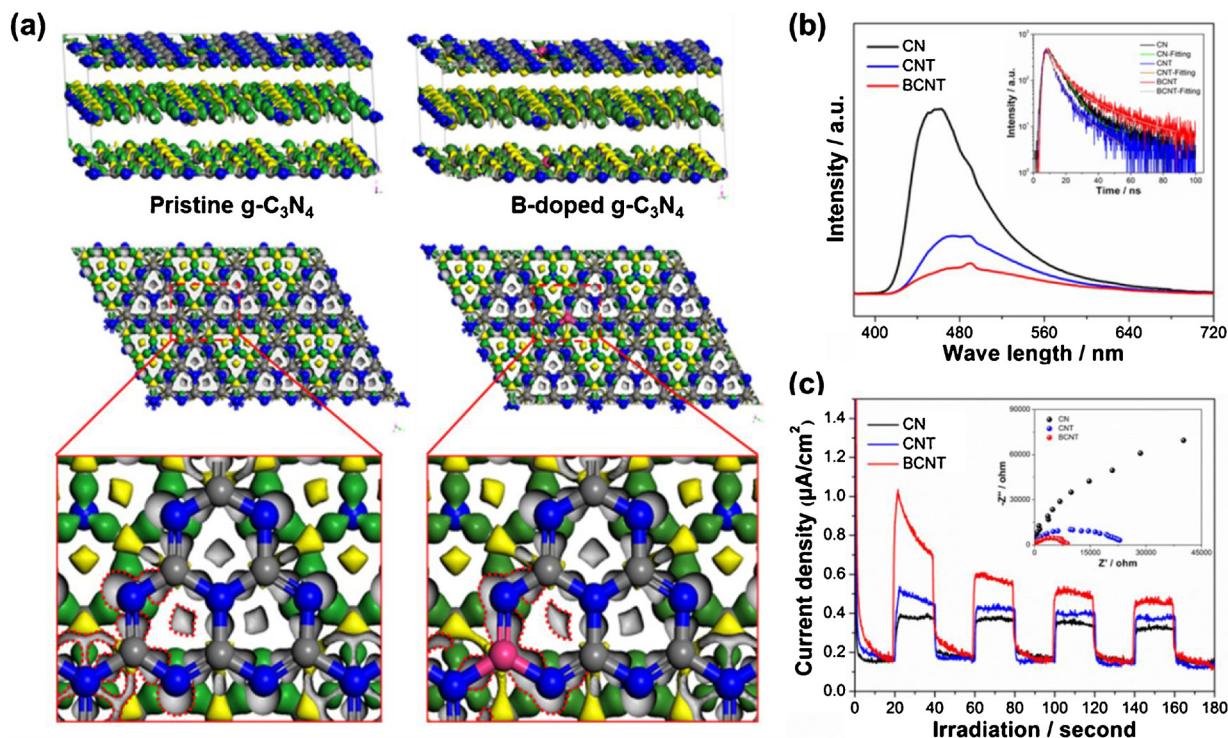

Fig. 4. (a) Calculated electron density difference diagram of the pristine g-C_3N_4 and B-doped g-C_3N_4 with a B atom doping concentration of 0.6% at the C1 site (yellow and green areas represent the increase and decrease of the electron density, respectively). (b) PL spectra (large inset) and time-resolved transient PL decay curves (small inset). (c) Transient photocurrent response (large inset) and Nyquist plots (small inset) of CN, CNT, and BCNT (For interpretation of the references to colour in this figure legend, the reader is referred to the web version of this article).

process, the electron density differences (EDDs) of pristine and B-doped supercell modes were calculated (Table S2, Fig. 4a). In pure g-C_3N_4, the C atom at the C1 site transferred 0.47 electrons to the neighboring N atoms. The electron density was further reduced after a C atom was substituted by a B atom at the C1 site, accumulating more electrons around the neighboring N atoms (B atom transferred 0.89 electrons to the neighboring N atoms). More importantly, simultaneously, electronic polarization effects were induced by the charge redistribution

Table 1

Results of the exponential decay-fitted parameters for the fluorescence lifetime of CN, CNT, and BCNT.

Samples	A_1 (%)	A_2 (%)	τ_1 (ns)	τ_2 (ns)	τ_{ave} (ns)
CN	100	—	7.29	—	7.29
CNT	67.59	32.41	4.34	19.22	14.46
BCNT	50.62	49.38	6.19	22.66	19.06

around the boron. This increased the intensity of the internal electric field, promoting the separation of the electron-hole pairs.

Photoluminescence (PL) emission can indicate the band-to-band electron-hole recombination in a semiconductor. The PL measurements showed that CNT exhibits an obvious decay compared to CN, which indicated the lower electron-hole recombination rate from the formation of a tubular structure and thinner layers (Fig. 4b). Furthermore, the

photoluminescence intensity was further quenched after the boron doping. In order to quantitatively evaluate the photo-generated charge carrier lifetime of CN, CNT and BCNT, time-resolved PL spectroscopy was utilized (small inset in Fig. 4b). The respective kinetic parameters after the multi-exponential fitting are listed in Table 1, in which the average lifetime, τ_{ave}, was calculated using Eq. (B1) [53]:

$$\tau_{ave} = \frac{A_1\tau_1^2 + A_2\tau_2^2}{A_1\tau_1 + A_2\tau_2} \tag{B1}$$

Where τ_1 and τ_2 are the emission lifetimes, and A_1 and A_2 are the corresponding amplitudes. The calculations showed that the average PL lifetime increased from 7.29 ns for CN to 14.46 ns for CNT, and eventually to 19.06 ns for BCNT. The obvious PL intensity quenching and prolonged PL lifetime of the CNT and BCNT samples indicated that the band-to-band recombination of electrons and holes was effectively suppressed after the introduction of the tubular structures and the B
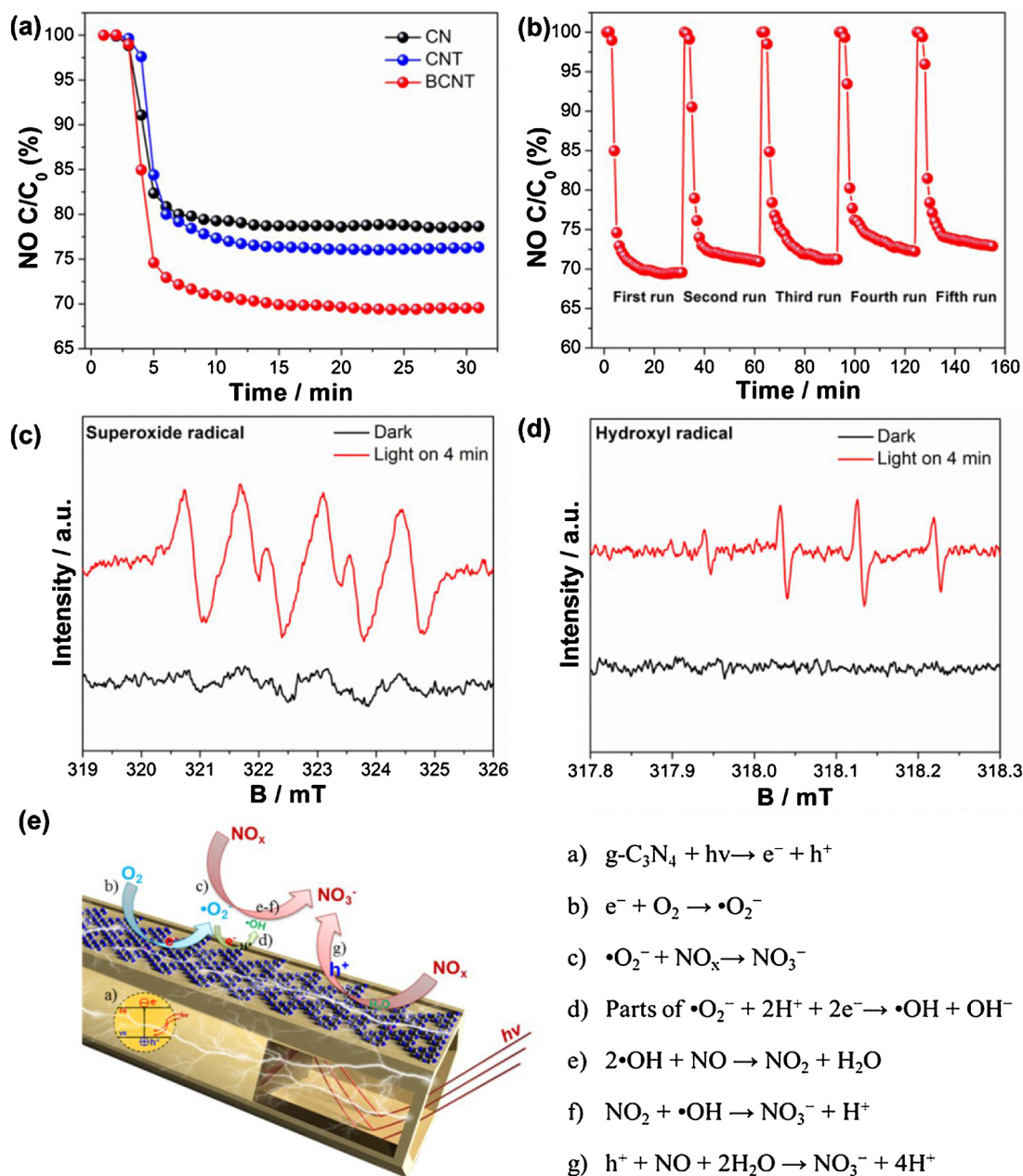

a) $g\text{-}C_3N_4 + h\nu \rightarrow e^- + h^+$

b) $e^- + O_2 \rightarrow \bullet O_2^-$

c) $\bullet O_2^- + NO_x \rightarrow NO_3^-$

d) Parts of $\bullet O_2^- + 2H^+ + 2e^- \rightarrow \bullet OH + OH^-$

e) $2\bullet OH + NO \rightarrow NO_2 + H_2O$

f) $NO_2 + \bullet OH \rightarrow NO_3^- + H^+$

g) $h^+ + NO + 2H_2O \rightarrow NO_3^- + 4H^+$

Fig. 5. (a) Visible light photocatalytic activities of CN, CNT, and BCNT for NO removal in air. (b) Cycling runs of BCNT. DMPO spin-trapping ESR spectra of BCNT (c) in methanol dispersion for DMPO-$\bullet O_2^-$ and (d) in aqueous dispersion for DMPO-$\bullet OH$. (e) Schematic diagram of the photocatalytic NO_x removal mechanisms with BCNT.

doping. In addition, electrochemical methods were implemented to further investigate the recombination and transport behaviors of the photo-induced carriers. Fig. 4c shows a comparison between the photocurrent-time curves for CN, CNT, and BCNT and the reproducible on-off cycles under visible-light irradiation. Compared to CN, the CNT sample exhibited an increased photocurrent response because of the hollow thin-layered tubular structure which can directly shorten the distance of electron diffusion from bulk to surface. The BCNT sample with a similar hollow tubular morphology showed the strongest photocurrent response, which showed that the separation rate of the photo-excited charge carriers was improved after the B-doping, in consistence with the conclusion of PL. However, the charge transport process occurring in the semiconductor in dark conditions can directly reflect its capacity to convey charge carriers to the targeted reactive sites [32,54]. This phenomenon is another critical factor for improving the performance of semiconductors. Thus, in order to further investigate the charge transport behavior of all samples, electrochemical impedance spectroscopy (EIS) measurements were carried out in dark conditions. As shown in Fig. 4c (small inset), the arc radius of CNT on the EIS Nyquist plot was smaller than that of CN. This result indicated that compared to random bulk nanoparticles with slow electron diffusion performance, the 1D tubular structures possess the advantage of facile charge carrier transport along the longitudinal dimensional structure [12,23]. In contrast, the arch radius of CNT was bigger than that of BCNT, suggesting that the substitution of C at the C1 site by a B atom enhanced the oriented transfer of charge carrier. These results support the DFT predictions and reveal that the proper use of B as a dopant did not only promote a more electron-hole effective separation. It also transferred the photo-excited charge carriers to the reactant molecules by adsorbing them on the active sites of the surface, which promoted them to involve in photocatalytic reactions.

3.5. Photocatalytic activity, stability, and mechanisms of NO removal and photocatalytic activity enhancement

Considering the aforementioned band gap engineering, electron-hole pair separation efficiency, and electron transfer ability, the photocatalytic performance of B-doped g-C_3N_4 tubes towards NO removal can be presumed superior than these of pure tubular g-C_3N_4 and bulk g-C_3N_4. The photocatalytic degradation of NO under visible-light irradiation in a continuous reactor is shown in Fig. 5a. The effects of NO adsorption equilibrium in dark and photolysis without photocatalyst under visible-light irradiation were excluded by performing controlled experiments (Fig. S11, Supporting information). In accord with the expected results, the BCNT sample showed the highest NO removal rate under visible-light irradiation (30.4%), which was 1.5 and 1.3 times higher than those of CN (20.8%) and CNT (22.9%), respectively. In addition, the by-products of NO_2 were monitored online and the selectivity of the reaction was calculated (Fig. S12, Supporting information). The results show that BCNT displayed the lowest conversion ratio of NO to NO_2, suggesting that it had an outstanding NO_2 inhibition ability. After single run reaction, the accumulated products on the surface of the BCNT sample were extracted by deionized water and measured by the ion chromatography (IC) method. It was found that the amounts of NO_3^- were 170.61 μg/g, but no NO_2^- was detected, which indicated that the oxidation of NO to NO_3^- was the major conversion process. Moreover, in order to examine the photocatalytic stability and durability, cycling runs on the photocatalytic removal of NO using BCNT were performed under the same conditions. As shown in Fig. 5b, the photocatalytic performance of BCNT can slightly decrease after five cycling because surface accumulation of nitrite occupied partial active sites. To examine the mechanism of NO removal with BCNT, the active radicals were detected using the electron spin-resonance spectroscopy (ESR) spin-trapping method. As shown in Fig. 5c and b, no signals were observed for $\cdot O_2^-$ and $\cdot OH$ in the dark in the beginning. After 4 min under visible-light irradiation, however, signals for both radicals

appeared clearly. In addition, the signals for the DMPO-$\cdot OH$ adduct were weaker than those of the DMPO-$\cdot O_2^-$ adduct. The fact that photo-generated holes of g-C_3N_4 could not directly oxidize H_2O to active species $\cdot OH$, [55,56] indicates that parts of $\cdot O_2^-$ turned into $\cdot OH$ radicals. Moreover, the fact that E_{VB} of the B-doped g-C_3N_4 (1.53 eV) was higher than that of HNO_3/NO (0.94 eV) meant that holes still play an important role in the NO removal by direct oxidation reaction. In order to further investigate the detailed adsorption behaviors of target molecules on the catalysts surface, the co-adsorption model of O_2, NO and H_2O on the surface of the B-doped g-C_3N_4 was established. Then, the charge transfer between B-doped g-C_3N_4 and O_2 was calculated by EDD and Mulliken Population Analysis. The results showed that 0.8 electrons transferred from the B-doped g-C_3N_4 to O_2, indicating that surface O_2 had the potential to form $\cdot O_2^-$. Besides, as shown in Fig. S13, the bonding effect between NO and O_2 was the sufficient evidence for the role of $\cdot O_2^-$ in the NO removal by direct oxidation reaction, but H_2O molecule had little effect. A more vivid schematic diagram of the photocatalytic NO_x removal mechanisms with BCNT is depicted in Fig. 5e.

Based on the DFT simulative results and characterizations analyses, the prepared B-doped g-C_3N_4 tubes exhibited enhanced visible-light-driven photocatalytic activity. Moreover, a mechanism of the NO photocatalytic oxidation was proposed. A B-atom substitution doping at the C1 site led to the enhanced visible-light harvesting ability and effective photo-induced charge carrier separation. This was caused by the narrower band-gap and electronic structure realignment of the B-substituted compound, which have proven to widen the visible-light absorption region and reduce the recombination of photo-generated electron-hole pairs. In addition, the tubular structure was found to increase the light-harvesting capacity through multiple reflections of incident light within the interior voids. Otherwise, the 1D tubular structure enhanced the charge carrier transport along the longitudinal dimension structure compared to that of random bulk nanoparticles with slow electron diffusion performance. The aforementioned factors induced the enhancement in the photocatalytic activity towards gaseous NO degradation under visible light.

4. Conclusion

In summary, we systematically applied DFT simulations as ideal guides to the design and, eventually, controlled synthesis of hollow B-doped g-C_3N_4 tubes using calcined melamine self-converted supramolecular precursors and boric acid. The prepared B-doped g-C_3N_4 hollow tubes exhibited the highest NO removal rate (30.4%) under visible-light irradiation from all tested compounds, which was 1.5 and 1.3 times higher than the values for bulk g-C_3N_4 (20.8%) and g-C_3N_4 hollow tubes (22.9%). This difference was mainly due to the superior light-harvesting, photo-generated electron-hole pair separation, and charge carrier transfer abilities of the new compound. This study provided a valuable design-fabrication pattern for g-C_3N_4 modification and engineering via DFT simulations. Moreover, a strategy was developed for the simultaneous foreign atom doping and architecture control of g-C_3N_4 via a self-assembly of supramolecular precursors.

152083/14E). Yu Huang was also supported by the "Hundred Talent Program" of the Chinese Academy of Sciences.

Appendix A. Supplementary data

Supplementary material related to this article can be found, in the online version, at doi:https://doi.org/10.1016/j.apcatb.2018.08.030.

References

[1] R.-J. Huang, Y. Zhang, C. Bozzetti, K.-F. Ho, J.-J. Cao, Y. Han, K.R. Daellenbach, J.G. Slowik, S.M. Platt, F. Canonaco, P. Zotter, R. Wolf, S.M. Pieber, E.A. Bruns, M. Crippa, G. Ciarelli, A. Piazzalunga, M. Schwikowski, G. Abbaszade, J. Schnelle-Kreis, R. Zimmermann, Z. An, S. Szidat, U. Baltensperger, I. El Haddad, A.S.H. Prevot, Nature 514 (2014) 218–222.
[2] P. Granger, V.I. Parvulescu, Chem. Rev. 111 (2011) 3155–3207.
[3] H. Chen, C.E. Nanayakkara, V.H. Grassian, Chem. Rev. 112 (2012) 5919–5948.
[4] Y. Huang, Y. Liang, Y. Rao, D. Zhu, J.J. Cao, Z. Shen, W. Ho, S.C. Lee, Environ. Sci. Technol. 51 (2017) 2924–2933.
[5] Z. Wang, S. Yan, Y. Sun, T. Xiong, F. Dong, W. Zhang, Appl. Catal. B: Environ. 214 (2017) 148–157.
[6] Y. Huang, D. Zhu, Q. Zhang, Y. Zhang, J.-j. Cao, Z. Shen, W. Ho, S.C. Lee, Appl. Catal. B: Environ. 234 (2018) 70–78.
[7] Y. Huang, Y. Gao, Q. Zhang, Y. Zhang, J.-j. Cao, W. Ho, S.C. Lee, J. Hazard. Mater. 354 (2018) 54–62.
[8] X. Wang, K. Maeda, A. Thomas, K. Takanabe, G. Xin, J.M. Carlsson, K. Domen, M. Antonietti, Nat. Mater. 8 (2009) 76–80.
[9] Z. Wang, Y. Huang, W. Ho, J. Cao, Z. Shen, S.C. Lee, Appl. Catal. B: Environ. 199 (2016) 123–133.
[10] W.J. Ong, L.L. Tan, Y.H. Ng, S.T. Yong, S.P. Chai, Chem. Rev. 116 (2016) 7159–7329.
[11] X. Li, J. Yu, M. Jaroniec, Chem. Soc. Rev. 45 (2016) 2603–2636.
[12] N. Wu, J. Wang, D.N. Tafen, H. Wang, J.G. Zheng, J.P. Lewis, X. Liu, S.S. Leonard, A. Manivannan, J. Am. Chem. Soc. 132 (2010) 6679.
[13] Y.M. Chen, Z. Li, X.W. Lou, Angew. Chem. 54 (2015) 10521–10524.
[14] G. Li, Z. Lian, W. Wang, D. Zhang, H. Li, Nano Energy 19 (2016) 446–454.
[15] H. Li, Z. Bian, J. Zhu, J. Am. Chem. Soc. 129 (2007) 8406–8407.
[16] G.K. Mor, K. Shankar, M. Paulose, O.K. Varghese, C.A. Grimes, Nano Lett. 6 (2006) 215–218.
[17] Z. Yang, Y. Zhang, Z. Schnepp, J. Mater. Chem. A Mater. Energy Sustain. 3 (2015) 14081–14092.
[18] X.H. Li, J. Zhang, X. Chen, A. Fischer, A. Thomas, M. Antonietti, X. Wang, Chem. Mater. 23 (2011) 4344–4348.
[19] Y.-S. Jun, E.Z. Lee, X. Wang, W.H. Hong, G.D. Stucky, A. Thomas, Adv. Funct. Mater. 23 (2013) 3661–3667.
[20] M. Shalom, S. Inal, C. Fettkenhauer, D. Neher, M. Antonietti, J. Am. Chem. Soc. 135 (2013) 7118–7121.
[21] Y.S. Jun, J. Park, S.U. Lee, A. Thomas, W.H. Hong, G.D. Stucky, Angew. Chem. Int. Ed. Engl. 52 (2013) 11083–11087.
[22] S. Guo, Z. Deng, M. Li, B. Jiang, C. Tian, Q. Pan, H. Fu, Angew. Chem. Int. Ed. Engl. 55 (2016) 1830–1834.
[23] Z. Tong, D. Yang, Y. Sun, Y. Nan, Z. Jiang, Small 12 (2016) 4093–4101.
[24] R. Asahi, T. Morikawa, T. Ohwaki, K. Aoki, Y. Taga, Science 293 (2001) 269–271.
[25] J. Liu, W. Li, L. Duan, X. Li, L. Ji, Z. Geng, K. Huang, L. Lu, L. Zhou, Z. Liu, W. Chen, L. Liu, S. Feng, Y. Zhang, Nano Lett. 15 (2015) 5137–5142.
[26] J. Fu, B. Zhu, C. Jiang, B. Cheng, W. You, J. Yu, Small 13 (2017).
[27] K. Wang, Q. Li, B. Liu, B. Cheng, W. Ho, J. Yu, Appl. Catal. B: Environ. 176-177 (2015) 44–52.
[28] C. Xu, Q. Han, Y. Zhao, L. Wang, Y. Li, L. Qu, J. Mater. Chem. A Mater. Energy Sustain. 3 (2015) 1841–1846.
[29] L. Z, W. X, Angew. Chem. 52 (2013) 1735-1738.
[30] N. Sagara, S. Kamimura, T. Tsubota, T. Ohno, Appl. Catal. B: Environ. 192 (2016) 193–198.
[31] Y. Zhang, T. Mori, J. Ye, M. Antonietti, J. Am. Chem. Soc. 132 (2010) 6294.
[32] R.J. Ran, T.Y. Ma, G. Gao, X. Du, S. Qiao, Energy Environ. Sci. 8 (2015) 3708–3717.
[33] G. Zhang, M. Zhang, X. Ye, X. Qiu, S. Lin, X. Wang, Adv. Mater. 26 (2014) 805–809.
[34] Q. Han, C. Hu, F. Zhao, Z. Zhang, N. Chen, L. Qu, J. Mater. Chem. A Mater. Energy Sustain. 3 (2015) 4612–4619.
[35] Z.-F. Huang, J. Song, L. Pan, Z. Wang, X. Zhang, J.-J. Zou, W. Mi, X. Zhang, L. Wang, Nano Energy 12 (2015) 646–656.
[36] H. Li, Y. Liu, X. Gao, C. Fu, X. Wang, ChemSusChem 8 (2015) 1189–1196.
[37] S.J. Clark, M.D. Segall, C.J. Pickard, P.J. Hasnip, M.I. Probert, K. Refson, M.C. Payne, Zeitschrift für Kristallographie-Crystalline Materials 220 (2005) 567–570.
[38] J.P. Perdew, K. Burke, M. Ernzerhof, Phys. Rev. Lett. 77 (1996) 3865.
[39] J.P. Perdew, M. Ernzerhof, K. Burke, J. Chem. Phys. 105 (1996) 9982–9985.
[40] H.J. Monkhorst, J.D. Pack, Phys. Rev. B 13 (1976) 5188.
[41] R.S. Mulliken, J. Chem. Phys. 23 (1955) 1833–1840.
[42] L. Kronik, Y. Shapira, Surf. Sci. Rep. 37 (1999) 1–206.
[43] H. Yu, R. Shi, Y. Zhao, T. Bian, Y. Zhao, C. Zhou, G.I.N. Waterhouse, L.Z. Wu, C.H. Tung, T. Zhang, Adv. Mater. (2017) 29.
[44] J.S. Shen, Q.G. Cai, Y.B. Jiang, H.W. Zhang, Chem. Commun. (Camb.) 46 (2010) 6786–6788.
[45] G. Arrachart, C. Carcel, P. Trens, J.J. Moreau, M. Wong, Chi Man, Chem. - Eur. J 15 (2009) 6279–6288.
[46] K.S.W. Sing, D.H. Everett, R.A.W. Haul, L. Moscou, R.A. Pierotti, J. Rouquerol, T. Siemieniewska, Pure Appl. Chem. 57 (1985) 603–619.
[47] L. Pan, S. Wang, W. Mi, J. Song, J.-J. Zou, L. Wang, X. Zhang, Nano Energy 9 (2014) 71–79.
[48] L. Lu, B. Wang, S. Wang, Z. Shi, S. Yan, Z. Zou, Adv. Funct. Mater. (2017) 27.
[49] N. Serpone, D. Lawless, R. Khairutdinov, J. Phys. Chem. 99 (1995) 16646–16654.
[50] H.-Y. Jiang, G. Liu, T. Wang, P. Li, J. Lin, J. Ye, RSC Adv. 5 (2015) 92963–92969.
[51] J. Zhang, X. Chen, K. Takanabe, K. Maeda, K. Domen, J.D. Epping, X. Fu, M. Antonietti, X. Wang, Angew. Chemie Int. Ed. English 49 (2010) 441–444.
[52] M. Zhou, J. Bao, Y. Xu, J. Zhang, J. Xie, M. Guan, C. Wang, L. Wen, Y. Lei, Y. Xie, ACS Nano 8 (2014) 7088–7098.
[53] Z. Zhang, Y. Huang, K. Liu, L. Guo, Q. Yuan, B. Dong, Adv. Mater. 27 (2015) 5906–5914.
[54] H. Xu, J. Yan, X. She, L. Xu, J. Xia, Y. Xu, Y. Song, L. Huang, H. Li, Nanoscale 6 (2014) 1406–1415.
[55] Z. Wang, W. Guan, Y. Sun, F. Dong, Y. Zhou, W.K. Ho, Nanoscale 7 (2015) 2471–2479.
[56] Z. Wang, Y. Huang, L. Chen, M. Chen, J. Cao, W. Ho, S.C. Lee, J. Mater. Chem. A Mater. Energy Sustain. 6 (2018) 972–981.